



**HAL**  
open science

## **GABRIELA : a new detector array for gamma-ray and conversion electron spectroscopy of transfermium elements.**

K. Hauschild, A.V. Yeremin, A. Lopez-Martens, O. Dorvaux, A.V. Belozarov, C. Briancon, M.L. Chelnokov, V.I. Chepigin, S.A. Garcia-Santamaria, V.A. Gorshkov, et al.

### ► To cite this version:

K. Hauschild, A.V. Yeremin, A. Lopez-Martens, O. Dorvaux, A.V. Belozarov, et al.. GABRIELA : a new detector array for gamma-ray and conversion electron spectroscopy of transfermium elements.. Nuclear Instruments and Methods in Physics Research Section A: Accelerators, Spectrometers, Detectors and Associated Equipment, 2006, 560, pp.388-394. 10.1016/j.nima.2006.01.107 . in2p3-00025590

**HAL Id: in2p3-00025590**

**<https://hal.in2p3.fr/in2p3-00025590>**

Submitted on 8 Feb 2006

**HAL** is a multi-disciplinary open access archive for the deposit and dissemination of scientific research documents, whether they are published or not. The documents may come from teaching and research institutions in France or abroad, or from public or private research centers.

L'archive ouverte pluridisciplinaire **HAL**, est destinée au dépôt et à la diffusion de documents scientifiques de niveau recherche, publiés ou non, émanant des établissements d'enseignement et de recherche français ou étrangers, des laboratoires publics ou privés.

# GABRIELA : a new detector array for $\gamma$ -ray and conversion electron spectroscopy of transfermium elements. <sup>\*</sup>

K. Hauschild <sup>a,\*</sup>, A.V. Yeremin <sup>b</sup>, O. Dorvaux <sup>c</sup>,  
A. Lopez-Martens <sup>a</sup>, A.V. Belozarov <sup>b</sup>, Ch. Briançon <sup>a</sup>,  
M.L. Chelnokov <sup>b</sup>, V.I. Chepigin <sup>b</sup>, S.A. Garcia-Santamaria <sup>a</sup>,  
V.A. Gorshkov <sup>b</sup>, F. Hanappe <sup>d</sup>, A.P. Kabachenko <sup>b</sup>,  
A. Korichi <sup>a</sup>, O.N. Malyshev <sup>b</sup>, Yu. Ts. Oganessian <sup>b</sup>,  
A.G. Popeko <sup>b</sup>, N. Rowley <sup>c</sup>, A.V. Shutov <sup>b</sup>, L. Stuttgé <sup>c</sup>,  
A.I. Svirikhin <sup>b</sup>

<sup>a</sup>*CSNSM, IN2P3-CNRS, F-91405 Orsay Campus, France*

<sup>b</sup>*Flerov Laboratory of Nuclear Reactions, JINR, 141 980 Dubna, Russia*

<sup>c</sup>*IReS, IN2P3-CNRS, F-67037 Strasbourg, France*

<sup>d</sup>*Université Libre de Bruxelles, C.P. 229, B-1050 Bruxelles, Belgium*

---

## Abstract

With the aid of the Geant4 Monte Carlo simulation package a new detection system has been designed for the focal plane of the recoil separator VASSILISSA situated at the Flerov Laboratory of Nuclear Reactions, JINR, Dubna. **GABRIELA** (**G**amma **A**lpha **B**eta **R**ecoil **I**nvestigations with the **E**lectromagnetic **A**nalyser VASSILISSA) has been optimised to detect the arrival of reaction products and their subsequent

radioactive decays involving the emission of  $\alpha$ - and  $\beta$ -particles, fission fragments,  $\gamma$ - and X-rays and conversion electrons. The new detector system is described and the results of the first commissioning experiments are presented.

*Key words:* Recoil separators; Decay tagging spectrometer; Alpha, gamma-ray, and conversion electron spectroscopy at recoil separators; GEANT Monte Carlo simulations;

*PACS:* , 23.60.+e, 27.80.+w, 29.30.Dn, 29.30.Kv

---

---

\* This project is jointly funded by the JINR and the IN2P3/CNRS. Work at the FLNR was performed partially under the financial support of the Russian Foundation for Basic Research, contract N 05-02-16198 and the JINR - BMBF (Germany), JINR - Polish and JINR - Slovak Cooperation Programmes.

\* Corresponding author.

*Email address:* `hauschild@csnsm.in2p3.fr` (K. Hauschild).

## 1 Introduction

The heaviest elements provide a unique laboratory to study nuclear structure and nuclear dynamics under the influence of large Coulomb forces and large mass ( $A$ ). The stability of nuclei beyond the spherical “doubly-magic”  $^{208}\text{Pb}$  ( $Z = 82$ ,  $N = 126$ ) decreases rapidly until the transfermium region ( $Z > 100$ ) where a lowering of the level density of single-particle states for nuclei in the neighbourhood of the deformed doubly-magic  $^{270}_{108}\text{Hs}$  reverses this trend locally [1]. However, the position of the spherical doubly-magic nucleus beyond  $^{208}\text{Pb}$  remains controversial : recent calculations predicting  $Z = 114$ ,  $120$ , or,  $126$  for the next magic proton shell, and  $N = 172$  or  $184$  for neutrons [2,3,4]. Among other things, this is a consequence of the treatment of the spin-orbit splitting. At large values of  $A$  a weakening of the spin-orbit splitting is predicted [5,6] which results in the lowering of orbitals with  $l = N$ ,  $j = l - \frac{1}{2}$ . The magnitude of this effect can either create or destroy stabilising gaps in the single-particle spectrum. For example, in various models the gap predicted at  $Z = 114$  depends highly on the  $2f_{7/2}$  and  $2f_{5/2}$  proton spin-orbit splitting. It is therefore crucial to determine the relative excitation energies of these single-particle states in the transfermium region [7] to reduce the extrapolation required in predicting the position of this “island of stability” for the very heaviest nuclei [8]. Recent reviews can be found in Refs. [9,10].

Beyond Einsteinium ( $Z=99$ ) detailed spectroscopic data is sparse. In both  $^{256}\text{Fm}$  [11] and  $^{255}\text{Fm}$  [12]  $\gamma$ -ray spectroscopy was performed after the chemical separation of reaction products following the irradiation of  $^{254}\text{Es}$  and  $^{253}\text{Es}$  targets respectively. Unfortunately further studies using this method are hin-

dered by a lack of suitable targets. Another method to populate the nuclei of interest is via heavy-ion fusion evaporation (HI,xn) reactions. In this case it is the overwhelming background from the predominant fission channel that needs to be addressed. This has been achieved with gas-jet transport systems and in-flight recoil separators. Recently spectroscopic studies in this mass region have seen intense activity in two distinct directions : 1) prompt in-beam spectroscopy at the target position exploiting the recoil decay tagging (RDT) method and, 2) isomeric, and, or, decay spectroscopy at the focal plane of the recoil separator. A number of rotational bands have now been observed using both  $\gamma$ -ray and conversion electron (CE) spectroscopy :  $^{254}\text{No}$  [13,14,15,16],  $^{252}\text{No}$  [18],  $^{253}\text{No}$  [15,17],  $^{250}\text{Fm}$  [19],  $^{251}\text{Md}$  [20] and  $^{255}\text{Lr}$  [21]. These results and additional unpublished data have been reviewed in [22]. However, focal plane decay studies using  $\alpha - \gamma$  coincidence measurements have only been reported for a few transfermium nuclei :  $^{251}\text{No}$  [23],  $^{253}\text{No}$  [22,24] and  $^{255}\text{Rf}$  [25]. The  $\alpha - \gamma$  coincidence, and,  $\alpha - \text{CE}$  coincidence decay spectroscopy of  $^{257}\text{No}$  [26] presents an interesting development with the re-emergence of gas-jet systems.

In these high  $Z$  nuclei the internal conversion becomes an extremely important decay mode since it can compete effectively with gamma decay. This makes it essential to perform electron spectroscopy and is the motivation behind the projects GREAT [27] and BEST, and, the subject of this paper, **GABRIELA**. In section 2 the salient features of the VASSILISSA set up will be presented. Then, in section 3, the modifications to the experimental set-up needed to perform detailed spectroscopy of excited states in transfermium nuclei are described along with the electronics developments required for the programme. Finally, some experimental results from commissioning runs will be shown to illustrate the performance of the GABRIELA system.

## 2 The VASSILISSA separator system

In the following section only a brief description of the VASSILISSA separator will be given. More details can be found in Ref [28,29].

The principal component of VASSILISSA consists of three electrostatic dipoles which separate spatially the trajectories of the recoiling nuclei, multinucleon transfer reaction products, fission fragments and beam particles by virtue of differences in their energies and ionic charges. An additional dipole magnet deflects the evaporation residues (ER's) by  $37^\circ$  improving the background suppression of the scattered beam by a factor of 10 - 50. This magnet also acts as a mass analyser [30,31]. Between the magnet and the separator system there is a 2 m thick concrete wall which provides substantial shielding from the beam dump. Downstream of the magnet a time-of-flight measurement is made and the ER's are then implanted into a  $300 \mu\text{m}$  thick, 16-strip,  $58 \times 58 \text{ mm}^2$  position sensitive Si detector at the focal plane of the separator (hereafter called the stop detector). Each strip is position sensitive in the vertical direction with a resolution of 0.3 - 0.5 mm (obtained from  $\alpha - \alpha$  correlations) and has a typical energy resolution of 20 keV for 5-10 MeV alpha particles. The subsequent position- and time-correlated alpha decays, characteristic of the implanted recoils, are also measured in the Si detector. The detection efficiency for these  $\alpha$  particles is around 50%.

### 3 GABRIELA

In order to perform gamma-ray and conversion-electron spectroscopy at the focal plane of VASSILISSA a number of modifications were needed. The Monte Carlo simulation code Geant4 [32] has been used as an aid to design an experimental set up with the goal of maximising the efficiency and resolution with a minimum of complexity. The set up is given in more details in the following subsections.

#### *3.1 Stop detector and support*

A new detector system, including a new more compact vacuum chamber optimised for transparency to  $\gamma$ -rays, was constructed to replace the old system which was used to measure alpha decay and spontaneous fission. The new aluminium chamber has a thickness of 6.5 mm, with the portion in front of the Ge detectors machined down to 2.5 mm, and an inner diameter of 160 mm. The support for the stop detector has been made from a single disc of stainless steel with cut-outs to allow cable connectors, cooling fluid feed-through, and, more importantly, an unobstructed view of the detector from the sides and from upstream. Fig. 1 shows a schematic view.

#### *3.2 Germanium detector array for $\gamma$ -ray spectroscopy*

The focal plane stop detector was surrounded by 7 Eurogam Phase-I Ge detectors [33] obtained from the French-UK loan pool. Six of these were placed inside BGO Compton shields and formed a ring around the detector cham-

ber with a focal point on the upstream (backwards) side of the stop detector (see Fig. 2). The distance from the centre of the stop detector to the front face of Ge crystal for these six detectors was about 130 mm. The aluminium back plate that closes the vacuum chamber was designed with an inset to enable the seventh Ge detector to be placed as close as possible to stop detector (about 35 mm). In the hollowed out portion the back plate is only 1.5 mm thick. The suppression shields served two purposes. The first of which is to improve the peak-to-total by vetoing events for which a  $\gamma$  ray Compton scatters out of the Ge detector which is indispensable for the identification of weak lines which would have otherwise been buried under the Compton background of more intense lines. The second is to reduce the counting rate from background radiation by vetoing events for which  $\gamma$  rays emitted from the concrete walls (mainly  $^{40}\text{K}$ ) interact in the germanium detectors. This enables increased “search” times to be used in the hunt for long lived isomers.

To obtain an absolute efficiency curve for  $\gamma$ -ray detection  $^{133}\text{Ba}$ ,  $^{152}\text{Eu}$  and  $^{241}\text{Am}$  sources of known activities were attached individually to the centre of an old stop detector which was then fixed to the detector support and inserted into the chamber. This permitted calibrations to be taken in conditions as close as possible to those during experimental runs. The sole difference being that the calibrations were performed with a point source, while experimental data is taken with the gamma-ray emitting recoils distributed almost uniformly over the surface of the stop detector. In Fig. 3a the measured  $\gamma$ -ray photo-peak efficiency from the calibration data is presented.

The reaction  $^{174}\text{Yb}(^{48}\text{Ca}, xn)^{222-x}\text{Th}$ , which is used primarily for alpha calibration purposes, can provide  $\gamma$  ray detection efficiency data under experimental conditions.  $^{217}\text{Th}$   $\alpha$  decays to  $^{213}\text{Ra}$ . A fraction of these decays populate ex-



cited states in  $^{213}\text{Ra}$  which, subsequently, decay to the ground state via  $\gamma$  emission [34]. From a comparison of the prompt  $\alpha - \gamma$  coincidence intensity ( $I(\alpha - \gamma)$ ) with the total  $\alpha$  singles spectrum ( $I(\alpha)$ ) one can determine the  $\gamma$  ray efficiency after correcting for internal conversion ( $\alpha_{TOT}$ ). That is :  $\epsilon_{\gamma} = I(\alpha - \gamma)/I(\alpha) \times (1 + \alpha_{TOT})$ . This measurement has also been carried out for the transfer product  $^{211}\text{Bi}$  which has fine-structure alpha decay to an excited state in  $^{207}\text{Tl}$ . These data, represented by the  $\Delta$  symbol in Fig.3a, are in agreement with the source data within errors. However, they do appear to indicate an experimental detection efficiency lower than that taken with calibration sources.

To examine the effect a distributed source has on the efficiency, Geant4 simulations have been performed for various  $\gamma$ -ray energies with  $\gamma$  rays emitted into  $4\pi$  from 1) a fixed point at the centre of the stop detector, and, 2) a uniform distribution over the x-y plane of the stop detector. The deposited energy recorded in the simulations was taken from the secondary electrons which are created by the Compton scattering and photoelectric processes. The results of these simulations are presented in Fig. 3b and indicate that an energy dependent scaling factor of 0.85 – 0.96 is needed to map the point source efficiency onto the distributed source efficiency. In order to obtain the excellent agreement between the measured and simulated efficiency curves every germanium crystal was shifted by 5 mm backwards within its aluminium housing relative to the nominal values given in Daresbury technical drawing A0-36/8813. This minor discrepancy is not that alarming since the precise dimensions and positions for the individual germanium crystals are not known.

For the above Germanium detector measurements new spectroscopy amplifiers and ADCs (4096 channels, 2  $\mu\text{s}$  conversion time) which accept a veto

signal were developed at the Flerov Laboratory. They demonstrated an excellent stability : during 1 month of measurements the omnipresent 1461 keV background line from  $^{40}\text{K}$  was observed to have a maximum energy shift of  $< \pm 0.03\%$  (0.4 keV). Within the energy range of 81 - 1408 keV the rms deviation of measured  $\gamma$ -ray energies compared to standard values [35] was found to be 0.1-, 0.2-, 0.2-, 0.2-, 0.2-, 0.2- and 0.1 keV for the 7 Ge detectors and indicates the precision to be expected in subsequent measurements. At 1332 keV a full width at half maximum (FWHM) of  $\sim 2.5$  keV was obtained.

### *3.3 Silicon detector array for conversion-electron spectroscopy*

In the backward direction of the stop detector an array of four 4-strip silicon detectors (Canberra PF-4CT-50\*50-500RM) are arranged in a tunnel configuration which is shown schematically in Fig. 1. Each detector has a total active area of  $50 \times 50 \text{ mm}^2$ , a thickness of  $500 \mu\text{m}$ , a front-face dead-layer thickness of  $< 25 \text{ nm}$  Si equivalent, and is mounted on a 1.6 mm thick,  $60 \times 120 \text{ mm}^2$  IS450 resin board manufactured by ISOLA. The pre-amplifiers (designed by GANIL) for each strip are mounted on the reverse side of this support board which is attached to a copper frame through which cooling fluid can be circulated. Thus the heating effect of the pre-amplifiers can be counteracted and the Si detectors cooled in order to reduce the resolution destroying leakage current.

The Si detectors are used to measure emitted particles escaping from the stop detector : principally conversion electrons, but also, alphas, fission fragments and betas. Due to the tunnel geometry a large proportion of these particles

will be detected at small distances upstream from the stop detector. The particles detected in the tunnel close to the stop detector will have suffered more straggling than those detected further upstream because, on average, they have travelled further in the stop detector. Therefore, Geant4 simulations were performed with the tunnel detectors being placed upstream from the stop detector at various distances to evaluate the compromise between the geometrical detection efficiency and spectral resolution. Dead layer thicknesses, support frames and epoxy boards for the silicon detectors and the vacuum chamber were included in the simulation geometry. Electrons were emitted into  $4\pi$  from an implantation depth of  $3.0(5) \mu\text{m}$  distributed uniformly over the x-y plane of the stop detector. The results of these simulations indicate that the effect of straggling has a much smaller effect on the energy resolutions compared to the degradation expected from the leakage current in the detectors and the electronics noise in the system. We have therefore tried to minimise the distance between the stop and tunnel detectors with the nominal distance between the epoxy support boards being about 2 mm.

Simulations have also been performed to investigate the efficiency and resolution as a function of recoil implantation depth. Using the geometry described above, with a 2 mm gap between the tunnel and stop detector supports, electrons were simulated to have been emitted from implantation depths of  $2.0(5)$ ,  $3.0(5)$ ,  $4.0(5)$ ,  $5.0(5)$  and  $6.0(5) \mu\text{m}$ . The results are given in Table 1 and can be broken into 3 regions : 1) For electron energies above 500 keV the performance of the set up is almost independent of the implantation depth for those depths simulated. 2) For energies between 100 and 400 keV there is a marginal difference in efficiency and a noticeable increase in FWHM with increasing implantation depth. 3) Below 100 keV there is a significant degradation in both

the detection efficiency and the resolution. In some simulations the effect of straggling was so large that peaks were no longer discernible and indicates that there is a limit below which one cannot perform electron spectroscopy in the tunnel detectors. This effect can be clearly seen in the simulations for 50 keV electrons shown in Fig. 4. The key to reducing this lower limit as far as possible is by placing a degrader foil in front of the stop detector in order to reduce the implantation depth.

Another important effect visible in Fig. 4, and presented in a more systematic manner in Table 1, is the shift in electron energy measured in the tunnel detectors. An energy calibration of the tunnel detectors must account for this shift. This can be achieved by either correcting unsealed source calibrations for the shifts given in Table 1, or, by implanting into the stop detector recoils known to decay via conversion electron emission and performing an in-beam calibration.

Before performing in-beam experiments initial calibrations with a  $^{133}\text{Ba}$  source were performed to align the Si electronics channels. Operating the Si detectors at  $-5^\circ\text{C}$  energy resolutions of between 8 - 10 keV FWHM were obtained for the 322-keV line, in-line with expectations when noise and leakage current affects are taken into account.

#### 4 Commissioning experiments

To test the new detectors and electronics a series of commissioning experiments were performed using the complete fusions reactions  $^{164}\text{Dy}(^{48}\text{Ca},xn)^{212-x}\text{Rn}$ ,  $^{174}\text{Yb}(^{40}\text{Ar},xn)^{214-x}\text{Ra}$  and  $^{181}\text{Ta}(^{40}\text{Ar},xn)^{221-x}\text{Pa}$  at beam energies correspond-

ing to the evaporation of 4 and 5 neutrons.

The first reaction was used to obtain an absolute efficiency measurement for the tunnel detectors. In  $^{207}\text{Rn}$  a  $13/2^+$  isomer at an excitation energy of 899 keV decays with a half-life of 181(18)  $\mu\text{s}$  to an intermediate  $9/2^-$  state at 665 keV which then decays to the  $5/2^-$  ground state [36]. This results in a  $\sigma L : E = \text{M2:234-keV}^1$  transition followed by an E2:665-keV line. Using coincidence measurements and singles intensities the following absolute efficiencies can be obtained :

$$1) \epsilon_{\gamma}(665) = I(234e^- \otimes 665\gamma) \times [1 + \alpha_{TOT}^{E2}(665)]/I_{e^-}^{singles}(234), \text{ and,}$$

$$2) \epsilon_{e^-}(665 - K) = I(234\gamma \otimes 665 - Ke^-) \times [1 + 1/\alpha_K^{E2}(665)]/I_{\gamma}^{singles}(234),$$

where  $I(E1e^- \otimes E2\gamma)$  represents the intensity observed for the coincidence measurement between an electron of energy  $E1$  and a  $\gamma$ -ray of  $E2$  and  $\alpha$  is the conversion coefficient. To reduce the possible contamination from other reaction channels all intensity measurements were taken in a time range  $32\mu\text{s} < \text{dT} < 1024\mu\text{s}$  with respect to the implantation of a recoil in the stop detector. The good agreement between the germanium array efficiency obtained from the  $e^- - \gamma$  coincidence,  $\epsilon_{\gamma}(665)$ , and the source measurements shown in Fig. 3a gives us confidence in the absolute efficiency determined for the tunnel detector which have also been obtained using the relationship :  $\epsilon_{e^-}(E : X) = I_{e^-}^{singles}(E : X) \times [1 + 1/\alpha_X(E)]/N_{isomer}$ , where, E is either 234- or 665-keV, X is either the K,L or M conversion electron and  $N_{isomer} = I_{\gamma}^{singles}(665) \times \alpha_{TOT}^{E2}(665)/\epsilon_{\gamma}(665)$ . These absolute efficiencies are presented in Fig. 5a and are in good agreement with the Geant4 simulations.

In Fig. 5b electron singles spectra are shown as an illustration of the quality

---

<sup>1</sup> Where  $\sigma$  represents either electric or magnetic radiation and  $L$  is the multipolarity and E is the transition energy.

of these data. The FWHM of the 234-K line ranges from 9.2- to 16.1 keV depending on the strip with most of the strips having a FWHM of 10 - 11 keV. The broadening of the lines with respect to the values quoted in Table 1 can be attributed to the detectors not being optimally cooled, an increase in noise during the U400 cyclotron operation and an implantation depth of  $> 4\mu\text{m}$  for these “low”  $Z$  recoils since the thickness of the degrader used was optimised for the higher  $Z$  transfermiums.

As an aside, these data have allowed a more accurate measurement of the half-life of the  $13/2^+$  isomer in  $^{207}\text{Rn}$ .  $\tau_{1/2} = 184.5(9)\mu\text{s}$  was obtained for the 234-K conversion-electron transition using the method described in Ref [37].

$\gamma$ -ray spectra obtained for an unsuppressed detector during the  $^{40}\text{Ar} + ^{174}\text{Yb} \rightarrow ^{214}\text{Ra}^*$  test run are shown in Fig. 6. The time difference between recoil and  $\gamma$ -ray detection as a function of measured  $\gamma$ -ray energy is plotted on an event-by-event basis in Fig. 6b. Different lifetimes for transitions depopulating the different isomeric states are clearly visible.  $\gamma$ -ray transitions detected within  $40\mu\text{s}$  after the recoil implantation are shown in Fig. 6c. In Table 2 the apparent half-lives of these  $\gamma$ -rays measured in the current work are given. In view of the agreement obtained for the half-lives of  $8^+$  isomers in  $^{210}\text{Ra}$  and  $^{212}\text{Ra}$  compared to the published values ( $2.28(8)\mu\text{s}$  cf  $2.24, 2.1(1),$  and  $2.36(4)\mu\text{s}$  [38,39,40], and  $9.1(7)\mu\text{s}$  cf  $10.5, 10.9(4)$  [40,41], respectively) the discrepancy between our measured value of  $9.7(6)\mu\text{s}$  and the value reported in Ref. [40] of  $4.0(5)\mu\text{s}$  for the  $(13/2^+)$  isomer in  $^{211}\text{Ra}$  needs independent confirmation.

## 5 Conclusion and Perspectives

The characteristics of the new GABRIELA detector array have been presented. This array, designed with the aid Geant4 simulations, has been installed at the focal plane of the VASSILISSA separator at the FLNR in Dubna. It has been constructed with the goal of performing detailed spectroscopic studies in transfermium nuclei. Following commissioning tests in May and June of 2004, two one-month-long experimental campaigns were performed in September - October 2004 and October 2005. The complete fusion reactions  $^{48}\text{Ca} + ^{207,208}\text{Pb} \rightarrow ^{255,256}\text{No}^*$  and  $^{48}\text{Ca} + ^{209}\text{Bi} \rightarrow ^{255}\text{Lr}^*$  were investigated. The decays of the isotopes  $^{253-255}\text{No}$ ,  $^{255}\text{Lr}$  and their daughter products are currently being analysed.

## References

- [1] Z. Patyk and A. Sobiczewski, Nucl. Phys. A 533 (1991) 132.
- [2] S. Cwiok, J. Dobaczewski, P.-H. Heenen, P. Magieski and W. Nazarewicz, Nucl. Phys. A 611 (1996) 211.
- [3] M. Bender, K. Rutz, P.-G. Reinhard, J.A. Maruhn and W. Greiner, Phys. Rev. C 60 (1999) 034304
- [4] A.T. Kruppa, M. Bender, W. Nazarewicz, P.-G. Reinhard, T. Verste and S. Cwiok, Phys. Rev. C 61 (2000) 034313
- [5] A. Bohr and B Mottelson, Nuclear Structure Vol. 1 (Benjamin, New York, 1969).
- [6] G. Mairle, Z. Phys. A 350 (1995) 285.

- [7] R.R. Chasman, and I. Ahmad, Phys. Letts B 392 (1997) 255.
- [8] A.V. Afanasjev, T.L. Khoo, S. Frauendorf, G.A. Lalazissis, and I. Ahmad, Phys. Rev. C 67 (2003) 024309.
- [9] M. Leino and F. Heßberger, Annu. Rev. Nucl. Part. Sci. 54 (2004) 175.
- [10] S. Cwiok, P.-H. Heenen and W. Nazarewicz, Nature 433 (2005) 705.
- [11] H.L. Hall, *et al.*, Phys. Rev. C 39 (1989) 1866.
- [12] I. Ahmad, R.R. Chasman, and P.R. Fields, Phys. Rev. C 61 (2000) 044301.
- [13] P. Reiter, *et al.*, Phys. Rev. Lett. 82 (1999) 509.
- [14] M. Leino, *et al.*, Eur. Phys. J. A 6 (1999) 63.
- [15] P.A. Butler, *et al.*, Phys. Rev. Lett. 89 (2002) 202501.
- [16] R.D. Humphreys *et al.*, Phys. Rev. C 69 (2004) 064324.
- [17] P. Reiter, *et al.*, Phys. Rev. Lett. 95 (2005) 032501.
- [18] R.-D. Herzberg, *et al.*, Phys. Rev. C 65 (2001) 014303.
- [19] R.-D. Herzberg, *et al.*, Proc. Int. Conf. Frontiers of Nuclear Structure (Berkeley, USA, 29 July 2002) AIP Conf. Proc. 656 (2003) 373.
- [20] A. Chatillon, *et al.*, private communication.
- [21] P.T. Greenlees, *et al.*, private communication.
- [22] R.-D. Herzberg, J. Phys. G 30 (2004) R123.
- [23] F.P. Heßberger, *et al.*, Eur. Phys. J. A 22 (2004) 417.
- [24] F.P. Heßberger, *et al.*, Nucl. Instr. and Meth. B 204 (2003) 597.
- [25] F.P. Heßberger, *et al.*, Eur. Phys. J. A 12 (2001) 57.
- [26] M. Asai *et al.*, Phys. Rev. Letts. 95 (2005) 102502.



- [27] R.D. Page, *et al.*, Nucl. Instr. and Meth. B 204 (2003) 634.
- [28] A.V. Yeremin, *et al.*, Nucl. Instr. and Meth. B 126 (1997) 329.
- [29] O.N. Malyshev, *et al.*, Nucl. Instr. and Meth. A 440 (2000) 86.
- [30] A.G. Popeko, *et al.*, Nucl. Instr. and Meth. A 510 (2003) 371.
- [31] O.N. Malyshev, *et al.*, Nucl. Instr. and Meth. A 516 (2004) 529.
- [32] S. Agostinelli, *et al.*, Nucl. Instr. and Meth. A 506 (2003) 250.
- [33] C. Beausang, *et al.*, Nucl. Instr. and Meth. A 313 (1992) 37.
- [34] F.P. Hessberger, *et al.*, Eur. Phys. J. A 15 (2002) 335.
- [35] R.B. Firestone, V.S. Shirley, C.M. Baglin, S.Y. Frank Chu, J. Zipkin, Table of Isotopes (John Wiley & Sons, New York, Chicester, Brisbane, Toronto, Singapore, 1996).
- [36] I. Rezanka, I.M. Ladenbauer-Bellis, J.O. Rasmussen, Phys. Rev. C 10 (1974) 766.
- [37] M. Leino, *et al.*, Phys. Rev. C 24 (1981) 2370.
- [38] J.F. Cocks and JUROSPHERE Collaboration, J. Phys. G 25 (1999) 839.
- [39] J.J. Ressler, *et al.*, Phys. Rev. C 69 (2004) 034331.
- [40] F.P. Hessberger, S. Hofmann, I. Kojouharov and D. Ackermann, Eur. Phys. J. A 22 (2004) 253.
- [41] T. Kohno, *et al.*, Phys. Rev. C 33 (1986) 392.

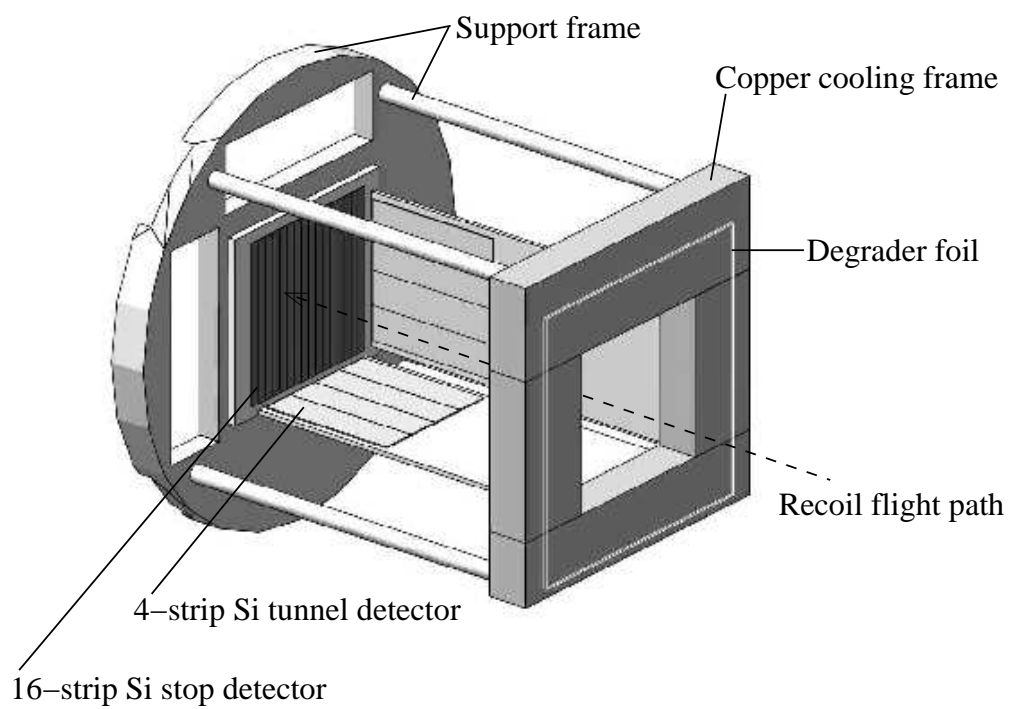


Fig. 1. Schematic view of the Si stop and tunnel detector set-up at the focal plane of VASSILISSA. Two sides of the tunnel have been removed for clarity.

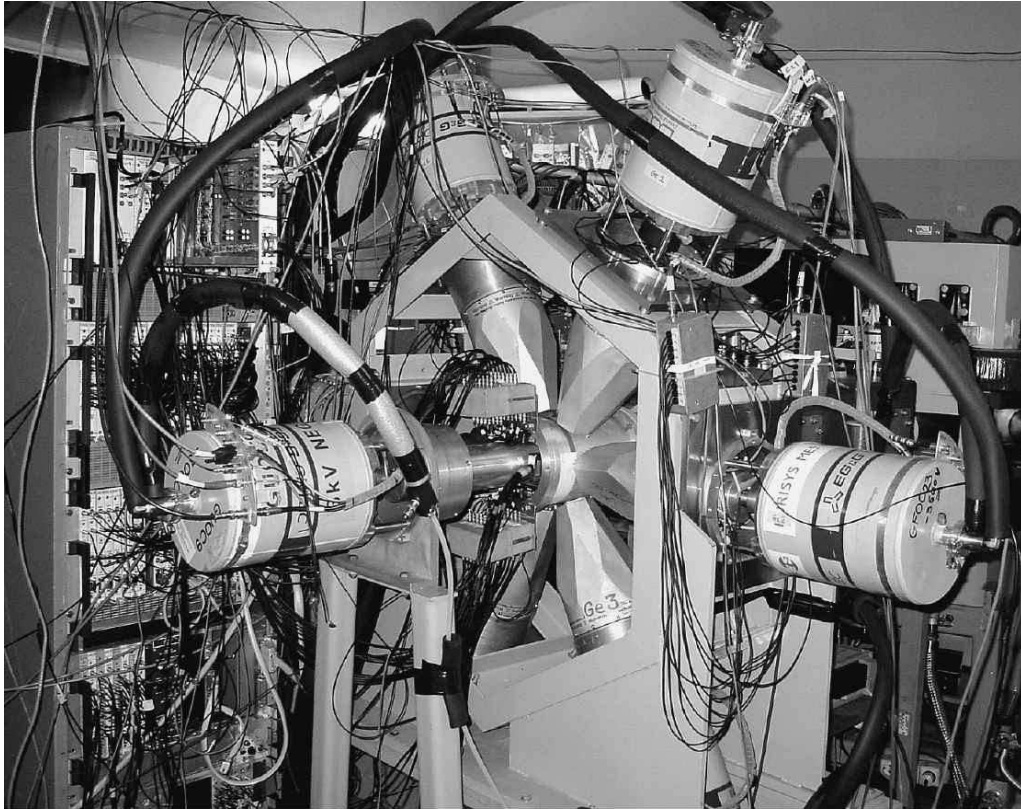


Fig. 2. Photograph of the GABRIELA set-up at the focal plane of VASSILISSA.

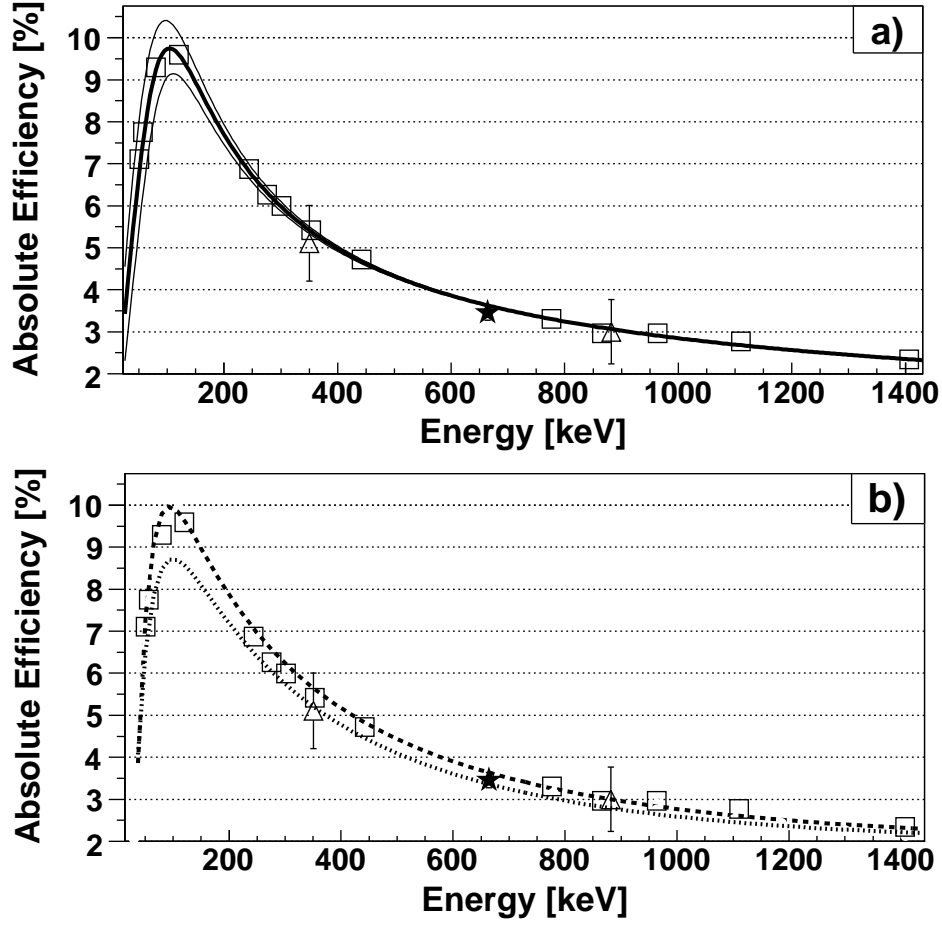


Fig. 3. Absolute efficiency curve for the 7 Ge detectors. ■ : measured using  $^{133}\text{Ba}$ ,  $^{152}\text{Eu}$  and  $^{241}\text{Am}$  sources; ★ measured using  $\gamma$ -electron coincidences from the decay of an isomeric state in  $^{207}\text{Rn}$  implanted into the stop detector using the reaction  $^{164}\text{Dy}(^{48}\text{Ca},5n)$ ;  $\Delta$  measured using  $\alpha$ - $\gamma$  coincidences from the fine-structure decay of  $^{211}\text{Bi}$  [ $E_\gamma = 351\text{-keV}$ ] and  $^{217}\text{Th}$  [ $E_\gamma = 882\text{-keV}$ ]. a) the bold solid line : fit to the data using the expression  $\log(\epsilon) = [(A + Bx_1 + Cx_1^2)^{-G} + (D + Ex_2 + Fx_2^2)^{-G}]^{-1/G}$  where  $x_1 = E_\gamma/100$  and  $x_2 = E_\gamma/1000$ ; the thin solid lines represent the error in the fit. b) dashed line : Geant4 simulated efficiency curve for a point source positioned at the centre of the stop detector; dotted line : Geant4 simulated efficiency curve for a distributed source.

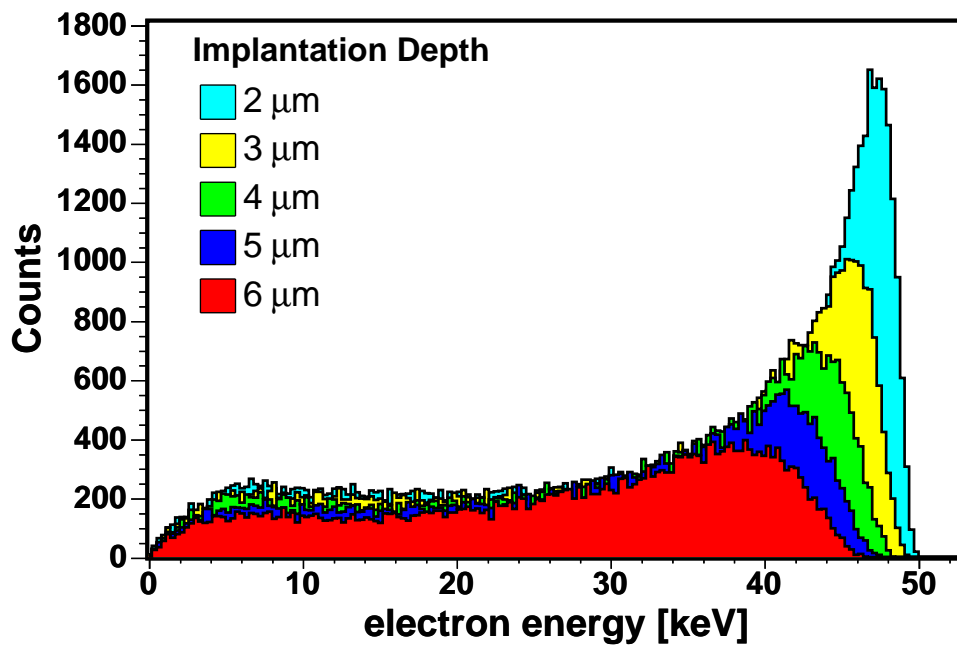


Fig. 4. Simulated energy deposited in the tunnel detectors for a 50 keV electron emitted from varying implantation depths within the stop detector.

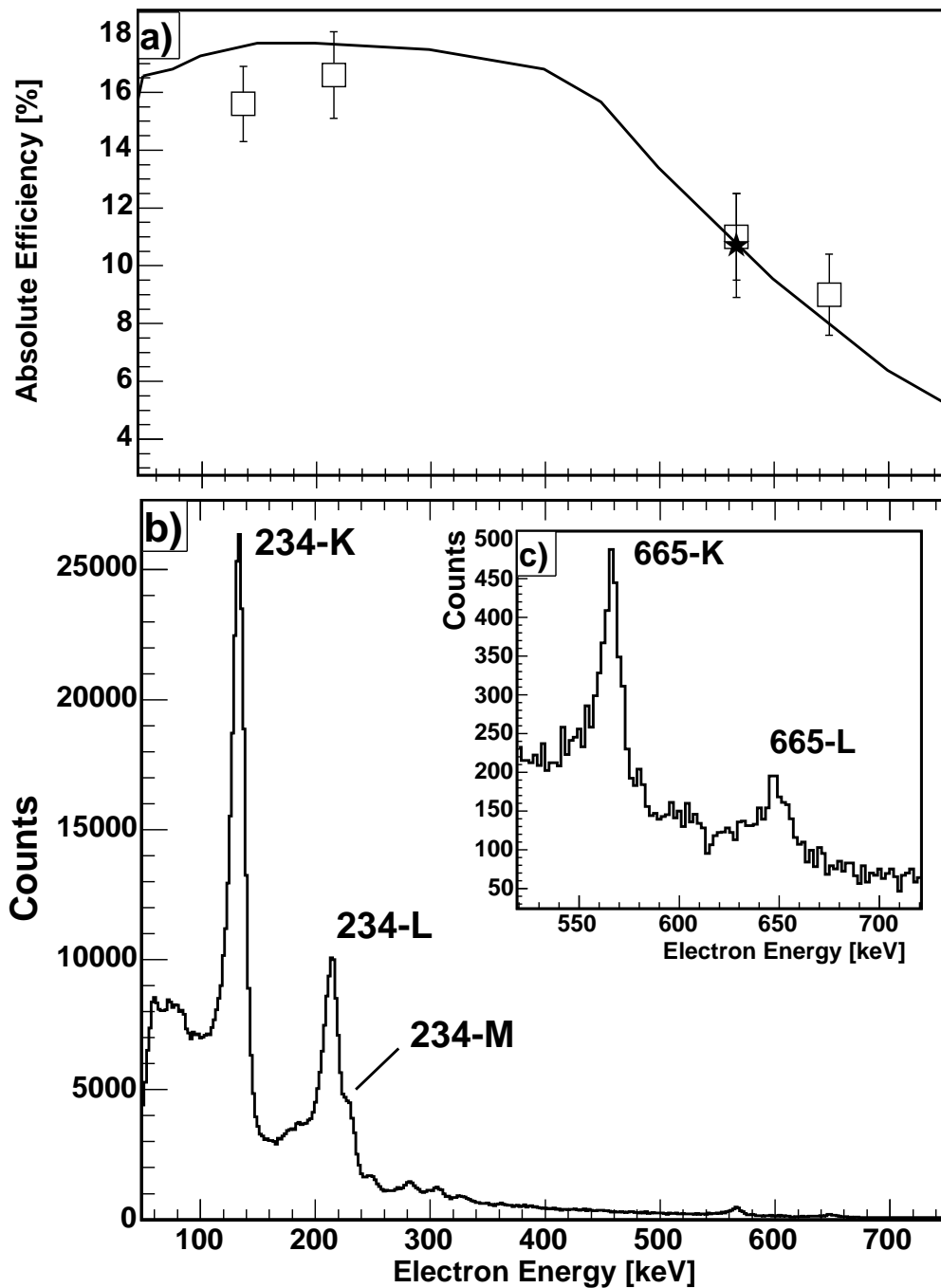


Fig. 5. a) Absolute efficiency curve for the 4 Si conversion electron detectors.  $\star$  : efficiency for the 567-keV (665 K conversion) obtained from  $\gamma$ -conversion electron coincidence measurements following the decay of the  $13/2^+$  isomer in  $^{207}\text{Rn}$ ;  $\square$  : singles efficiency measurements from the same  $^{207}\text{Rn}$  data; the bold solid line : results of Geant4 simulations with an implantation depth of  $3.0(5) \mu\text{m}$  distributed uniformly in the x-y plane of the stop detector. b) Electron singles spectra measured in the tunnel detectors within the time range  $32 \mu\text{s} < \text{dT} > 1024 \mu\text{s}$  of a recoil from the reaction  $^{48}\text{Ca} + ^{164}\text{Dy}$  being detected in the stop detector. c) The inset shows the high energy part of the spectrum.

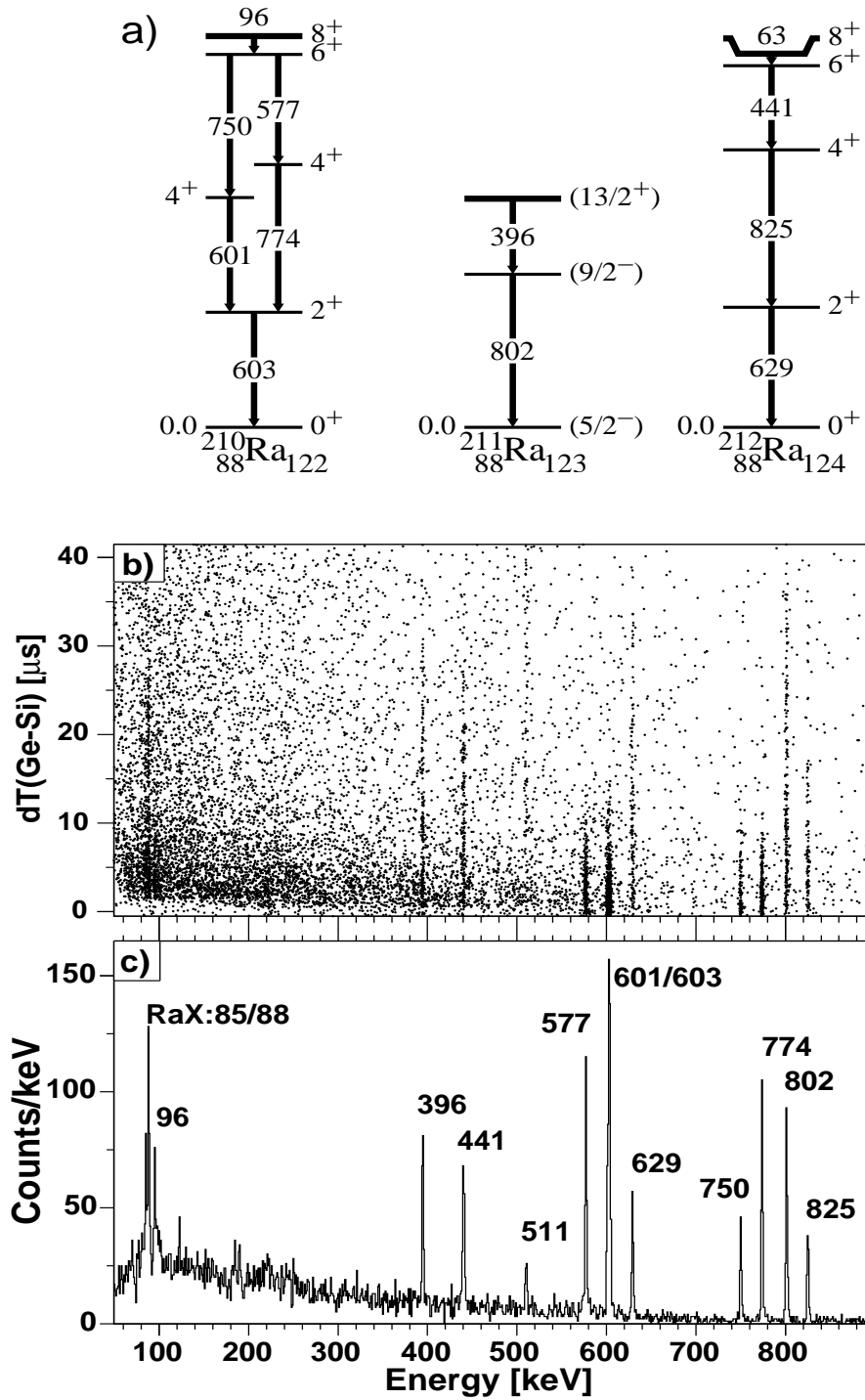


Fig. 6. a) Partial level schemes (taken from Refs. [38,39,40,41]) below the isomeric states in the Radium isotopes populated via the  $^{174}\text{Yb}(^{40}\text{Ar},xn)^{214-x}\text{Ra}$  reaction and transported to the focal plane of VASSILISSA. b) The time difference between recoil and  $\gamma$ -ray detection as a function of measured  $\gamma$ -ray energy is plotted on an event-by-event basis. c) Delayed  $\gamma$ -ray transitions observed within  $40 \mu\text{s}$  after the recoil was detected.

Table 1

Results of Geant4 simulations with different “recoil” implantation depths in the stop detector. For each simulation  $2 \times 10^5$  electrons were emitted into  $4\pi$  from points distributed uniformly in the x-y plane of the stop detector. The depth in the stop detector at which the electrons were emitted was taken to be a Gaussian distribution with a sigma of  $0.5 \mu\text{m}$ .  $\Delta E$  is the difference between the emitted electron energy and the energy measured in a tunnel detector (ie the energy deposited in the stop detector). The efficiency,  $\epsilon$ , was determined by integrating the simulated spectrum between  $\pm 3\sigma$  of the full energy centroid. The error bars on  $\epsilon$  are  $< 0.2\%$  and arise from the error in determining the integration limits. The effect of electronics noise is not included.

depth ( $\mu\text{m}$ )	electron energy											
	30 keV			40 keV			50 keV			75 keV		
	$\Delta E$ (keV)	fwhm (keV)	$\epsilon$ %	$\Delta E$ (keV)	fwhm (keV)	$\epsilon$ %	$\Delta E$ (keV)	fwhm (keV)	$\epsilon$ %	$\Delta E$ (keV)	fwhm (keV)	$\epsilon$ %
2.0(5)	4.6	8.2(1.3)	13.8	3.2	6.3(0.5)	16.4	2.2	4.1(1)	16.8	1.5	2.7(2)	17.0
3.0(5)	7.8	9.1(2.2)	7.6	5.3	8.3(1.1)	14.8	3.8	6.2(3)	16.5	2.6	3.9(3)	16.8
4.0(5)	–	–	–	8.0	9.3(0.2)	11.2	5.9	8.8(6)	15.8	3.5	5.4(5)	16.7
5.0(5)	–	–	–	11.1	12(2)	8.9	8.1	9.1(8)	13.1	4.7	6.6(2)	16.2
6.0(5)	–	–	–	–	–	–	10.7	13.6(2)	10.2	6.0	8.2(8)	15.1
depth ( $\mu\text{m}$ )	100 keV			200 keV			300 keV			400 keV		
	$\Delta E$ (keV)	fwhm (keV)	$\epsilon$ %	$\Delta E$ (keV)	fwhm (keV)	$\epsilon$ %	$\Delta E$ (keV)	fwhm (keV)	$\epsilon$ %	$\Delta E$ (keV)	fwhm (keV)	$\epsilon$ %
	2.0(5)	1.2	2.2(1)	17.3	0.7	1.4(1)	17.5	0.5	1.2(1)	17.6	0.6	1.1(1)
3.0(5)	2.0	3.4(1)	17.1	1.3	2.3(1)	17.5	1.0	2.0(1)	17.3	0.9	1.7(1)	16.8
4.0(5)	2.8	4.3(4)	16.6	1.8	3.0(1)	17.3	1.5	2.5(2)	17.1	1.3	2.2(2)	16.5
5.0(5)	3.6	5.1(3)	16.3	2.3	3.5(3)	16.8	1.8	3.0(2)	16.8	1.7	2.7(2)	16.4
6.0(5)	4.5	6.0(6)	16.0	2.8	4.0(3)	16.3	2.3	3.3(3)	16.3	2.0	3.2(2)	16.2
depth ( $\mu\text{m}$ )	500 keV			600 keV			700 keV			800 keV		
	$\Delta E$ (keV)	fwhm (keV)	$\epsilon$ %	$\Delta E$ (keV)	fwhm (keV)	$\epsilon$ %	$\Delta E$ (keV)	fwhm (keV)	$\epsilon$ %	$\Delta E$ (keV)	fwhm (keV)	$\epsilon$ %
	2.0(5)	0.4	1.1(1)	13.8	0.5	1.0(1)	9.5	0.5	1.0(1)	6.3	0.4	0.9(1)
3.0(5)	0.8	1.6(1)	13.4	0.8	1.5(1)	9.5	0.7	1.4(2)	6.2	0.7	1.3(2)	4.1
4.0(5)	1.2	2.1(2)	13.4	1.1	1.9(2)	9.3	1.0	1.9(2)	6.2	1.0	1.7(2)	4.1
5.0(5)	1.5	2.5(2)	13.4	1.4	2.4(1)	9.3	1.4	2.3(2)	6.1	1.3	2.2(3)	4.0
6.0(5)	1.9	2.8(2)	13.0	1.8	2.8(3)	9.2	1.7	2.6(3)	6.2	1.6	2.5(3)	4.0



Table 2

Apparent half-lives of the transitions involved in the decay of isomeric states in  $^{210}\text{Ra}$ ,  $^{211}\text{Ra}$  and  $^{212}\text{Ra}$ .

$^{210}\text{Ra}$		$^{211}\text{Ra}$		$^{212}\text{Ra}$	
$E_\gamma$ [keV]	$T_{1/2}$ [ $\mu\text{s}$ ]	$E_\gamma$ [keV]	$T_{1/2}$ [ $\mu\text{s}$ ]	$E_\gamma$ [keV]	$T_{1/2}$ [ $\mu\text{s}$ ]
96	2.51(31)	396	9.5(8)	441	8.9(9)
750	2.57(32)	802	9.9(8)	825	7.7(1.3)
577	2.37(17)			629	10.2(1.0)
774	2.34(17)				
601/603	2.15(11)				